JGP Journal of General Physiology

RESEARCH ARTICLE

A bilobal model of Ca^{2+}-dependent inactivation to probe the physiology of L-type Ca^{2+} channels

Worawan B. Limpitikul[1], Joseph L. Greenstein[2], David T. Yue[1], Ivy E. Dick[1,3]*, and Raimond L. Winslow[2]*

L-type calcium channels (LTCCs) are critical elements of normal cardiac function, playing a major role in orchestrating cardiac electrical activity and initiating downstream signaling processes. LTCCs thus use feedback mechanisms to precisely control calcium (Ca^{2+}) entry into cells. Of these, Ca^{2+}-dependent inactivation (CDI) is significant because it shapes cardiac action potential duration and is essential for normal cardiac rhythm. This important form of regulation is mediated by a resident Ca^{2+} sensor, calmodulin (CaM), which is comprised of two lobes that are each capable of responding to spatially distinct Ca^{2+} sources. Disruption of CaM-mediated CDI leads to severe forms of long-QT syndrome (LQTS) and life-threatening arrhythmias. Thus, a model capable of capturing the nuances of CaM-mediated CDI would facilitate increased understanding of cardiac (patho)physiology. However, one critical barrier to achieving a detailed kinetic model of CDI has been the lack of quantitative data characterizing CDI as a function of Ca^{2+}. This data deficit stems from the experimental challenge of uncoupling the effect of channel gating on Ca^{2+} entry. To overcome this obstacle, we use photo-uncaging of Ca^{2+} to deliver a measurable Ca^{2+} input to CaM/LTCCs, while simultaneously recording CDI. Moreover, we use engineered CaMs with Ca^{2+} binding restricted to a single lobe, to isolate the kinetic response of each lobe. These high-resolution measurements enable us to build mathematical models for each lobe of CaM, which we use as building blocks for a full-scale bilobal model of CDI. Finally, we use this model to probe the pathogenesis of LQTS associated with mutations in CaM (calmodulinopathies). Each of these models accurately recapitulates the kinetics and steady-state properties of CDI in both physiological and pathological states, thus offering powerful new insights into the mechanistic alterations underlying cardiac arrhythmias.

Introduction

L-type voltage-gated calcium channels (LTCCs) are critical conduits for calcium (Ca^{2+}) entry into many excitable cells, including skeletal muscle, cardiomyocytes, and neurons. In ventricular cardiomyocytes, the principal LTCC is the $Ca_V1.2$ channel, which plays a major role in both shaping the action potential and triggering Ca^{2+} release from the SR, leading to myocyte contraction (Bodi et al., 2005). Disruption of the normal function of this channel has been linked to multiple disorders, including severe forms of long-QT syndrome (LQTS; Crotti et al., 2013; Limpitikul et al., 2014, 2017; Yin et al., 2014; Dick et al., 2016) and heart failure (Ikeda et al., 2009). To properly perform these critical roles, $Ca_V1.2$ channels use two major forms of feedback regulation: voltage-dependent inactivation (VDI) and Ca^{2+}-dependent inactivation (CDI). Of these, CDI is believed to play a dominant role in sculpting action potential morphology (Sun et al., 1997; Morotti et al., 2012). Thus, accurate knowledge of the quantitative details of CDI progression is of critical importance to understanding normal cardiac physiology.

The mediator of CDI in $Ca_V1.2$ is the ubiquitously expressed Ca^{2+} sensor calmodulin (CaM), which is known to preassociate with the carboxy tail of the channel in its Ca^{2+}-free form (apoCaM; Erickson et al., 2001; Pitt et al., 2001; Mori et al., 2004). A channel bound to apoCaM exhibits relatively high open probability upon voltage-mediated activation, known as mode 1 gating (Imredy and Yue, 1994). Upon Ca^{2+} binding, Ca^{2+}/CaM departs from its preassociation site, resulting in a reduction of the channel open probability (mode Ca gating; Imredy and Yue, 1994; Zühlke et al., 1999). Ca^{2+}/CaM remains associated with the channel via Ca^{2+}/CaM effector sites within the amino and carboxy termini of the channel (Ben Johny et al., 2013). Moreover, CaM has the remarkable ability to respond differentially to Ca^{2+} originating from distinct spatial sources. This feature is enabled

[1]Calcium Signals Laboratory, Department of Biomedical Engineering, The Johns Hopkins University School of Medicine, Baltimore, MD; [2]Institute for Computational Medicine, Department of Biomedical Engineering, The Johns Hopkins University, Baltimore, MD; [3]Department of Physiology, University of Maryland School of Medicine, Baltimore, MD.

Dr. David T. Yue died on December 23, 2014; *I.E. Dick and R.L. Winslow contributed equally to this paper; Correspondence to Ivy E. Dick: ied@som.umaryland.edu; Raimond L. Winslow: rwinslow@jhu.edu.

© 2018 Limpitikul et al. This article is distributed under the terms of an Attribution–Noncommercial–Share Alike–No Mirror Sites license for the first six months after the publication date (see http://www.rupress.org/terms/). After six months it is available under a Creative Commons License (Attribution–Noncommercial–Share Alike 4.0 International license, as described at https://creativecommons.org/licenses/by-nc-sa/4.0/).

Check for updates

Downloaded from http://rupress.org/jgp/article-pdf/150/12/1688/1798053/jgp_201812115.pdf by guest on 09 February 2026

by the bilobal design of CaM, where a single molecule consists of two semi-independent lobes, each capable of binding Ca^{2+} with different affinities and using differing kinetic schemes to achieve selectivity for a particular source of Ca^{2+} (Dick et al., 2008; Tadross et al., 2008). Specifically, the C-lobe of CaM invariably senses the fluctuation of the local Ca^{2+} concentration at the mouth of the channel, whereas the N-lobe is capable of functioning in two different modes depending on the channel context. For many Ca^{2+} channels, the N-lobe of CaM responds to the cytosolic Ca^{2+} level arising from the cumulative effect of multiple Ca^{2+} sources. However, for $Ca_V1.2$, the N-lobe acts primarily as a local sensor; although the underlying mechanism for this local selectivity differs from that of the C-lobe (Dick et al., 2008; Tadross et al., 2008). This bilobal scheme plays an important role in physiology. However, the extent of cooperativity between the two lobes remains to be determined.

Disruption of the function of either lobe of CaM has been linked to severe cardiac phenotypes including LQTS and catecholaminergic polymorphic ventricular tachycardia (Crotti et al., 2013; Yin et al., 2014), known as calmodulinopathies. In particular, multiple mutations within the C-lobe of CaM are associated with a frequently lethal form of LQTS (Limpitikul et al., 2014, 2017). In each case, the mutation results in a decrease in Ca^{2+} binding affinity to the C-lobe of CaM, causing a significant reduction in CDI within myocytes harboring the mutation. Thus, full understanding of both normality and pathophysiology requires consideration of the bilobal regulation of CaM on $Ca_V1.2$.

Given the importance of CDI to physiological function, numerous in silico models have been used to gain a more in-depth understanding of how CDI plays a role in the context of the cardiac action potential. To date, several methods have been deployed to model the CDI of cardiac $Ca_V1.2$ channels. One method involves treating both VDI and CDI as canonical Hodgkin and Huxley gates, dependent on voltage or Ca^{2+} concentration, respectively; that is, total Ca^{2+} current is a product of conductance, VDI "gate," CDI "gate," and a driving force based on the Goldmann–Hodgkin–Katz equation (Hund and Rudy, 2004; ten Tusscher et al., 2004; ten Tusscher and Panfilov, 2006). Building on this, a second method includes Markovian models containing closed, open, and inactivated states. Here, rate constants for the transition into a fraction of the inactivated states depend on voltage (representing VDI), whereas transitions into the remaining inactivated states depend on Ca^{2+} concentration (representing CDI). Importantly, most of these models do not incorporate the allosteric mechanism of CDI, where Ca^{2+}-inactivated channels maintain the ability to open, but with a reduced (yet nonzero) open probability (Faber et al., 2007; Mahajan et al., 2008). A few models have partially addressed this issue; however, even in most of these models, the majority of inactivation is carried by VDI, in contrast to the known physiological mechanism of $Ca_V1.2$ channels (Jafri et al., 1998; Decker et al., 2009). In attempting to capture these distinct CDI kinetics, some have included the addition of two time constants for CDI (Hund and Rudy, 2004; O'Hara et al., 2011), yet the bilobal response of $Ca_V1.2$ remains unexplored. Moreover, Greenstein and Winslow (2002) and Greenstein et al. (2006) demonstrated that the proper physiological balance between CDI and VDI (in which LTCC inactivation is strongly dominated by CDI), and hence the proper relationship between CDI strength and action potential morphology, can be achieved in simulations in which LTCCs are localized to independently functioning cardiac dyads within a myocyte. Although all of these approximations of $Ca_V1.2$ inactivation can indeed produce Ca^{2+} current (I_{Ca}) with kinetics grossly resembling experimental I_{Ca} recorded during an action potential, they do not take into account the allosteric and bilobal nature of CaM regulation of $Ca_V1.2$, thus limiting their utility in describing $Ca_V1.2$ gating in response to variable spatial calcium signals (Sun et al., 1997; Dick et al., 2008; Tadross et al., 2008).

One obstacle to the development of accurate CDI models is a paucity of experimental data. As $Ca_V1.2$ becomes permeable to the Ca^{2+} ions that modulate its own opening, it is challenging to accurately control and measure the amount of Ca^{2+} that preassociated CaM actually senses. Moreover, during an action potential, there is at least a ∼10-fold difference in Ca^{2+} concentration between the dyadic space facing the channel pore and the rest of the cytoplasm (Neher, 1998). Most experimental values of Ca^{2+} used to drive or validate the CDI models are measured by cytosolic Ca^{2+}-sensitive fluorescence dyes, where the readout represents the average of bulk (global) and subspace (local) Ca^{2+} concentrations. To accurately measure the Ca^{2+} sensed by a CaM residing on a channel, we take advantage of photo-uncaging (Lipp et al., 1996) to deliver a controlled amount of Ca^{2+} to the channels, while simultaneously monitoring the cytosolic concentration of Ca^{2+}, a method that has been validated in the context of both L-type and P/Q-type Ca^{2+} channels (Tadross et al., 2013; Lee et al., 2015; Dick et al., 2016). As we allow the Ca^{2+} cage to fully dialyze before the photolysis, this Ca^{2+} measurement will accurately represent both the bulk and local Ca^{2+} concentration.

Using this technique, we recorded CDI for each lobe of CaM individually and resolved the kinetic response to measured levels of Ca^{2+}. This new high-resolution data enabled the creation of a four-state model for independent N- or C-lobe–mediated CDI. Our models successfully recapitulate both the kinetic and steady-state properties of CDI for each lobe. Next, we considered the integrated effect of bilobal CaM on $Ca_V1.2$ CDI. Using experimental CDI measurements for wild-type CaM (CaM_{WT}), we constructed a 16-state model of bilobal CaM regulation. Not only can this full model effectively capture both the kinetics and steady-state behavior of CDI under physiological conditions, but it also recapitulates the behavior of calmodulinopathic CaM. Thus, this CDI model could prove to be an invaluable asset in understanding both physiological and pathological states of $Ca_V1.2$ regulation.

Materials and methods

Molecular biology

The $Ca_V1.2$ channel used in this study was made up of the human α_{1C} cardiac isoform corresponding to Acc# Z34810 within the pcDNA3 vector. The original channel backbone was a gift from T.W. Soong (National University of Singapore, Singapore; Tang et al., 2004) and was modified as previously described (Dick et al., 2016) to conform to the desired cardiac isoform. The point mutation E736A (in the S6 helix of domain II; Ellinor et al., 1995) was introduced using standard overlap extension PCR, resulting in a

Downloaded from http://rupress.org/jgp/article-pdf/150/12/1688/1798053/jgp_201812115.pdf by guest on 09 February 2026

Ca^{2+} channel with increased selectivity for Li^{+} ($Ca_V1.2^{E2A}$; Ellinor et al., 1995; Dick et al., 2016). The altered selectivity and decrease of pore block for this channel was previously determined (Ellinor et al., 1995; Dick et al., 2016).

Engineered rat brain CaM_{12}, CaM_{34}, and CaM_{1234}, in which the aspartate-to-alanine mutations were introduced in the EF hands of N-lobe, C-lobe, and both lobes, respectively, were gifts from John P. Adelman (Vollum Institute, Portland, OR). The LQTS CaM_{D130G} mutation was generated using QuikChange site-directed mutagenesis (Agilent) on rat brain CaM (M17069) in the pcDNA3 vector (Invitrogen). Both WT and engineered CaMs were cloned into the pIRES2-ECFP vector, modified from pIRES2-EGFP (Clontech Laboratories), using NheI and BglII, thus allowing visualization of positively transfected cells.

Transfection of HEK293 cells

HEK293 cells were cultured on glass coverslips in 10-cm dishes. α_{1C} along with its auxiliary subunits β_{2a} (M80545) and $\alpha_2\delta$ (NM012919.2) were transiently transfected along with either WT or mutant CaM using a standard calcium phosphate method (Peterson et al., 1999). 8 µg of each plasmid was used, along with 2 µg of simian virus 40 T antigen complementary DNA to ensure robust expression.

Whole cell electrophysiology

Whole-cell voltage-clamp recordings of HEK293 cells were performed at room temperature 1–2 d after transfection. Recordings were obtained using an Axopatch 200B amplifier (Axon Instruments). Whole-cell voltage-clamp records were digitally sampled at 10 kHz and low-pass filtered at 5 kHz. P/8 leak subtraction was used, with series resistances of 1–2 MΩ. Experiments were performed in external solutions containing (in mM) 80 TEA-$MeSO_3$, 10 HEPES, pH 7.4, 80 LiCl, and 2 EGTA at 300 mOsm adjusted with glucose. Internal solutions contained (in mM) 135 CsCl, 40 HEPES, pH 7.4, 1–2 citrate, either 5 µM Fluo-2 (TefLabs) + 5 µM Fluo-2 Low Affinity (TefLabs) or 10 µM Fluo-4FF (Invitrogen), 2.5 µM Alexa Fluor 568 (Invitrogen), 2 DMNP-EDTA (Invitrogen), and 0.25–1 $CaCl_2$. Measurement of CDI was done in response to a 0-mV step depolarization, which is close to the peak of the current–voltage relationship for all combinations of channel and CaM coexpression (Supplementary text, Co-expression of engineered CaM).

During current recordings, Ca^{2+} concentration was simultaneously measured optically using Ca^{2+} indicator dyes. To ensure proper quantification of Ca^{2+} at various levels, we selected Ca^{2+} dyes with variable Ca^{2+} affinities as required for the range of Ca^{2+} measured. For all Ca^{2+} steps <10 µM, we used an internal solution containing the mixture (see above) of Fluo-2 Low Affinity (K_d = 6.7 µM) and Fluo-2 High Affinity (K_d = 230 nM). This allowed clear resolution of low basal Ca^{2+} (pre-flash) as well as the ability to distinguish even small or moderate Ca^{2+} steps (post-flash; Lee et al., 2015). This enhanced range of Ca^{2+} measurements permitted precise measurement of the time-varying Ca^{2+} concentration after the flash, allowing our model to account for the kinetic changes in both Ca^{2+} and CDI. To obtain accurate measurements of Ca^{2+} steps in the range >10 µM, Fluo-4FF (K_d = 9.7 µM) was used (Dick et al., 2016). To decrease the variability across experiments, each dye mixture was premixed in a large stock and used throughout the study. Calibration of premixed stocks of Fluo-2/Alexa was performed by Lee et al. (2015) and Fluo-4FF/Alexa by Dick et al. (2016). The dyes were excited with a 514-nm argon laser, via a 545DCLP dichroic mirror and either a 545/40BP (Fluo) or 580LP (Alexa Fluor 568) filter. Fluorescence intensity was measured via photomultiplier tubes at a sampling frequency of 10 kHz. Brief UV pulses used to produce Ca^{2+} steps were generated by a Cairn UV flash photolysis system. The amount of Ca^{2+} delivered to channels was controlled by adding different ratios of $CaCl_2$ to DM-nitrophen (DMN) in the pipette solution and varying the UV intensities achieved by adjusting the voltage (50–200 V) and total capacitance (500–4,000 µF) of the flash photolysis system.

Data are presented as mean ± SEM. Statistical analysis of the data was performed using Prism 5 (GraphPad). To compare the CDI response to the level of intracellular Ca^{2+} concentration for each experimental condition, CDI as a function of Ca^{2+} was fitted with Hill equations, and the extra sum-of-squares F test was used to determine statistically significant difference among the K_d values.

Computational simulations

Experimentally measured or apparent CDI was a combination of true CDI and residual Ca^{2+} pore block of $Ca_V1.2^{E2A}$ channel (Fig. 1, A–D). Careful characterization of this residual pore block allows quantification of the magnitude of true CDI (Supplementary text, Derivation of apparent and true CDI) which is used in all computational simulations. For N-lobe, C-lobe, and bilobal models of CDI, a set of ordinary differential equations (ODEs) was used to represent the probability of being in each state (Figs. 3 A, 4 A, and 5 A), with the sum of all probabilities constrained to be 1. Detailed equations are described in the Supplementary text, Differential equations for N-lobe and C-lobe CDI and Differential equations for bilobal CDI. All simulations were performed using Matlab (MathWorks). ODEs were solved using Matlab function *ode23t*. The measured Ca^{2+} concentration was fitted with a double exponential equation, and this idealized Ca^{2+} signal was used as a model input (Supplementary text, Model setup and parameter optimization). Model optimization was performed by using Matlab function *patternsearch* to minimize the error between experimental and simulated current (Supplementary text, Model setup and parameter optimization). Parameter constraints for all models are described in detail in Supplementary information, Parameter constraints.

Online supplemental information

The supplemental text describes the effect of co-expression of engineered CaM on voltage dependence of $Ca_V1.2$ channel activation; contains derivation of true and apparent CDI; contains differential equations describing N-lobe and C-lobe CDI; contains describing differential equations for bilobal CDI; contains model setup and a detailed method for parameter optimization; describes parameter constraints; demonstrates the importance of cooperativity factors in the bilobal CDI model; contains derivation of cooperativity between CaM lobes; and describes parameter sensitivity. Fig. S1 shows the current–voltage relationship

Downloaded from http://rupress.org/jgp/article-pdf/150/12/1688/1798053/jgp_201812115.pdf by guest on 09 February 2026

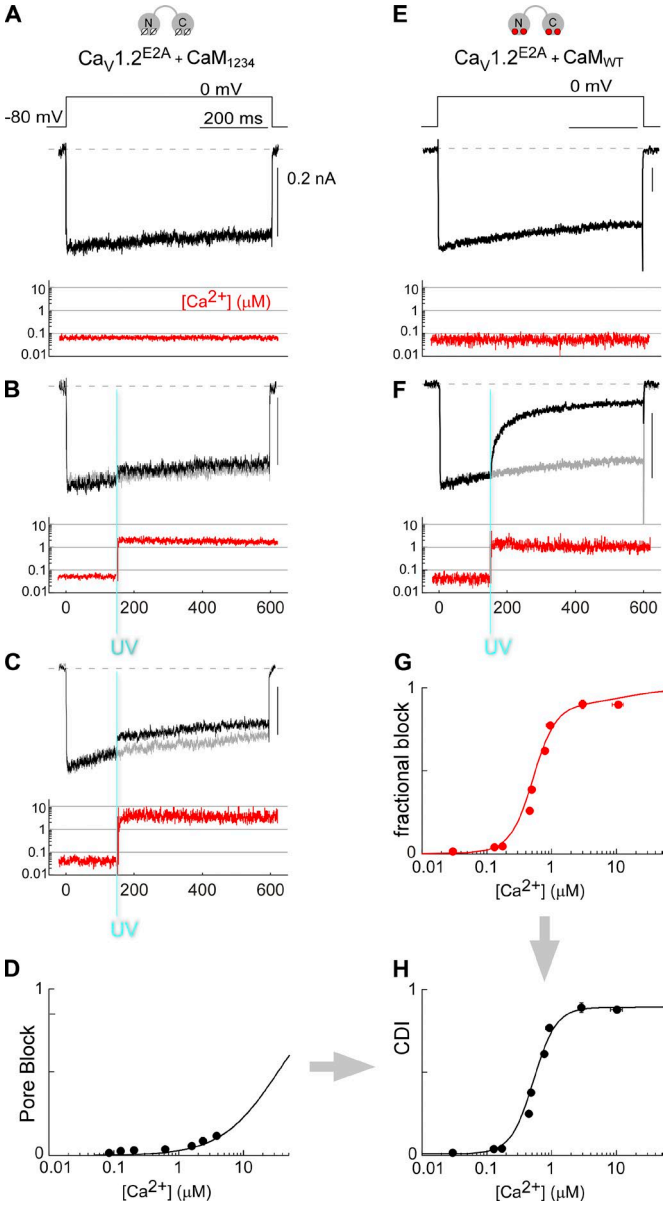

Figure 1. **Using photo-uncaging to quantify CDI. (A–D)** $Ca_V1.2^{E2A}$ channels are coexpressed with mutant CaM_{1234} in HEK293 cells to characterize pore block. **(A)** Li^+ currents before Ca^{2+} uncaging (black) with simultaneously measured resting $[Ca^{2+}]$ (red). **(B)** UV photo-uncaging of Ca^{2+} (blue) results in a step increase in $[Ca^{2+}]$ (red) and minimal reduction of Li^+ current (black) compared with preflash conditions (gray). **(C)** Li^+ current recorded before (gray) and after (black) UV photo-uncaging of Ca^{2+}. A higher-intensity UV flash results in a larger Ca^{2+} step (red), compared with B, yet there is a small decrease in current, indicating minimal pore block in this channel. **(D)** Steady-state pore block as a function of $[Ca^{2+}]$, fitted with a Hill coefficient of 1 and large K_d of 33 μM (black curve). Data are from 13 replicates (variable level UV flashes) across 7 cells. Error bars indicate ±SEM. **(E–H)** CDI from $Ca_V1.2^{E2A}$ coexpressed with CaM_{WT}. **(E)** Li^+ current (black) at resting $[Ca^{2+}]$ (red; F) UV flash produces a large Ca^{2+} step (red) and concurrent reduction in current (black) indicative of CDI. Gray trace shows preflash current. **(G)** Fractional block of current after UV flash as a function of $[Ca^{2+}]$. Data represent the binned average from 14 replicates (variable level UV flashes) in seven cells. Error bars indicate ±SEM. **(H)** Removal of pore block (D) from the data in G allows the resolution of true CDI as a function of $[Ca^{2+}]$. Steady-state CDI as a function of $[Ca^{2+}]$, fitted with a Hill coefficient of 2.5 and K_d of 0.52 μM.

for $Ca_V1.2^{E2A}$. Fig. S2 shows a schematic of CDI measurement as a function of $[Ca^{2+}]$. Fig. S3 shows a method for idealization of $[Ca^{2+}]$. Fig. S4 shows a cost function schematic. Fig. S5 shows model results in the absence of cooperativity. Fig. S6 shows evaluation of parameter sensitivity in the N-lobe model. Fig. S7 shows evaluation of parameter sensitivity in the C-lobe model. Fig. S8 shows evaluation of parameter sensitivity in the bilobal model. Table S1 shows $[Ca^{2+}]$ parameters used in model simulations. Table S2 shows quantification of the sensitivity of model parameters.

Results

Experimental quantification of CDI as a function of Ca^{2+}

To create a detailed kinetic model of CDI, we first need to obtain high-resolution CDI data for each lobe of CaM at known Ca^{2+} concentrations. To do this, we must overcome the experimental challenge of coupled Ca_V gating and Ca^{2+} entry, which we accomplished by adapting a previously described photo-uncaging method (Tadross et al., 2013; Lee et al., 2015; Dick et al., 2016). We use Li^+ as the charge carrier across the channel (Fig. 1 A), while controlling intracellular Ca^{2+} via the Ca^{2+} cage DMN. However, because of the high affinity of Ca^{2+} for the channel pore, intracellular Ca^{2+} has been shown to block the entry of monovalent ions in a process known as pore block (Ellinor et al., 1995). To mitigate this artifact, we used a previously described $Ca_V1.2$ channel in which the mutation E736A was inserted into the selectivity filter of domain II in the α_1 subunit of the $Ca_V1.2$ channel ($Ca_V1.2^{E2A}$), which shifts the selectivity of the channel in favor of Li^+ (Ellinor et al., 1995; Dick et al., 2016).

We are now able to deliver a spatially uniform concentration of intracellular Ca^{2+} such that measured bulk cytosolic Ca^{2+} is identical to that surrounding the CaM residing on the channel (Tadross et al., 2013; Lee et al., 2015; Dick et al., 2016). Specifically, during patch-clamp recording, we dialyzed DMN into HEK293 cells cotransfected with CaM and human cardiac $Ca_V1.2$ channels. Then, upon delivery of a UV pulse, the ester bonds of DMN are cleaved and Ca^{2+} is released into the cytosol. In this setting, the magnitude of the Ca^{2+} step delivered can be controlled by adjusting the intensity of the UV light and varying the ratio between Ca^{2+} and DMN in the dialysate (Figs. 1, B and C; Tadross et al., 2013; Lee et al., 2015; Dick et al., 2016). To measure the real-time concentration of Ca^{2+}, we added Ca^{2+}-sensitive dyes to the dialysate and simultaneously recorded the fluorescence intensity and Li^+ current (Fig. 1 A). Because the physiologically relevant range of Ca^{2+} is larger than the dynamic range of a single Ca^{2+} dye, we combined known ratios of low- and high-affinity Ca^{2+} dyes (Fluo-2 HighAff and Fluo-2 LowAff) to accurately measure $[Ca^{2+}]$ across the entire range (Lee et al., 2015).

To characterize the extent of any residual Ca^{2+} pore block in $Ca_V1.2^{E2A}$, we coexpressed the channel with CaM_{1234}, an engineered CaM in which the Ca^{2+} binding of all four EF hands has been disrupted (Dick et al., 2016). Under these conditions, Li^+ current displays a slow decay in current amplitude, indicative of VDI (Fig. 1 A). Upon Ca^{2+} photo-uncaging, a small instantaneous drop in current demonstrates the remaining pore block of the

Downloaded from http://rupress.org/jgp/article-pdf/150/12/1688/1798053/jgp_201812115.pdf by guest on 09 February 2026

$Ca_V1.2^{E2A}$ channel (Fig. 1, B and C). This residual pore block can be quantified as:

$$f_{block} = 1 - \frac{\frac{I_{end,f}}{I_{preUV,f}}}{\frac{I_{end,nf}}{I_{preUV,nf}}}, \quad (1)$$

where I_{preUV} is current measured 20 ms before the UV pluses, I_{end} is current remaining at the end of the voltage step, and *nf* (no flash) and *f* (flash) represent current without and with UV flash delivered 150 ms after channel activation, respectively. For $Ca_V1.2^{E2A}$, f_{block} increases monotonically as a function of $[Ca^{2+}]$ (Fig. 1 D) and can be fitted with the Hill equation,

$$f_{block} = amp_{block} * \frac{[Ca]^{nHill}}{[Ca]^{nHill} + K_{d/block}^{nHill}}, \quad (2)$$

with amplitude (amp_{block}) = 1, Hill coefficient ($nHill$) = 1, and $K_{d/block}$ = 33 µM for Fluo-2/Alexa or 55 µM for Fluo-4FF/Alexa, which are comparable to previously described values (Ellinor et al., 1995; Dick et al., 2016).

This setup can now be used to probe the extent of CDI of $Ca_V1.2$ at various cytosolic levels of Ca^{2+}. When $Ca_V1.2^{E2A}$ is now coexpressed with wild-type CaM (CaM_{WT}), a step release of Ca^{2+} (Fig. 1 F, red) results in robust inactivation of the Li^+ current (Fig. 1 F, black) indicating CDI. Importantly, the confounding effects of VDI can be eliminated in two ways. First, we coexpressed our channels with the β_{2a} subunit, which is known to minimize the extent of VDI in the channel complex (Dafi et al., 2004). Second, we can eliminate any residual VDI by using the preflash current as our baseline for CDI measurements (Eq. 3). Further, by varying the amplitude of the Ca^{2+} step, we can quantify the extent of steady-state CDI as a function of Ca^{2+} (Fig. 1 G). Here, the normalized ratio of current reduction after Ca^{2+} delivery ($f_{CDI,app}$, Fig. 1 G) represents the combination of true CDI ($f_{CDI,true}$, Fig. 1 H) and residual pore block (f_{block}, Fig. 1 D):

$$f_{CDI,app} = 1 - \frac{\frac{I_{end,f}}{I_{preUV,f}}}{\frac{I_{end,nf}}{I_{preUV,nf}}} = 1 - (1 - f_{block}) * (1 - f_{CDI,true}) \quad (3)$$

(see Supplementary text, Derivation of apparent and true CDI). Thus, the true CDI can be calculated (Fig. 1 H) and fitted with a Hill equation of the form

$$f_{CDI} = CDI_{max} * \frac{[Ca]^{nHill}}{[Ca]^{nHill} + K_d^{nHill}}, \quad (4)$$

where $CDI_{max,WT}$ = 0.88, $nHill_{WT}$ = 2.5, and $K_{d,WT}$ = 0.52 µM (R^2 = 0.97), comparable to previously described values (Dick et al., 2016). Thus, we have a robust method for quantifying the extent of CDI in response to controlled concentrations of intracellular Ca^{2+}, providing data with which to optimize our in silico models.

Measurement of N- and C-lobe–mediated CDI

Prior studies have demonstrated separate forms of CDI mediated independently by the N- or C-lobe of CaM. Importantly, these two forms of CDI can respond to spatially distinct Ca^{2+} sources, each using different mechanistic schemes (Dick et al., 2008; Tadross et al., 2008). However, this unique feature of CaM is not represented in published in silico models of CDI. This lack of lobe-specific detail is, in large part, the result of limited data pertaining to each lobe of CaM. We therefore undertook detailed experimental characterization of N- and C-lobe–mediated CDI.

To begin, we use an engineered CaM (Keen et al., 1999), in which Ca^{2+} binding of the C-lobe is abolished (CaM_{34}), allowing the resolution of N-lobe–mediated CDI alone (Peterson et al., 1999). $Ca_V1.2^{E2A}$ coexpressed with CaM_{34} displays robust Li^+ current at baseline (Fig. 2 A). However, upon photo-uncaging of Ca^{2+}, the current decays exponentially (Fig. 2 B, black), with notably different kinetics compared with CaM_{WT} (Fig. 1 F). By varying the amount of Ca^{2+} delivered, we can describe the extent of steady-state N-lobe–mediated CDI as a function of intracellular Ca^{2+} (Fig. 2 C). This relationship can be fitted with a Hill equation (Eq. 4) with $CDI_{max,N}$ = 0.62, Hill coefficient $nHill_N$ = 1.8, and $K_{d,N}$ = 0.9 µM (R^2 = 0.79).

Similarly, CDI mediated by the C-lobe CaM can be probed by measuring Li^+ current through $Ca_V1.2^{E2A}$ coexpressed with an engineered CaM with restricted C-lobe–only Ca^{2+} binding (CaM_{12}; Keen et al., 1999). Here, photo-uncaging Ca^{2+} results in a rapid inactivation of the Li^+ current (Fig. 2 E, black) at a faster rate than in the presence of CaM_{34} (Fig. 2 B). Notably, this increased kinetic response of C-lobe CaM occurs at each level of Ca^{2+} measured. Moreover, steady-state CDI mediated by the C-lobe of CaM can also be fitted by a Hill equation (Eq. 4), with $CDI_{max,C}$ = 0.66, Hill coefficient $nHill_C$ = 1.4, and $K_{d,C}$ = 1.15 µM (R^2 = 0.93; P > 0.05 compared with $K_{d,N}$). Importantly, the K_d values obtained for N- and C-lobe CaM are each significantly larger than that obtained for CaM_{WT} (0.9, 1.15, and 0.5 µM respectively, P < 0.0001).

CaM lobe-specific models of CDI

Having achieved robust experimental measurements of CDI mediated by each lobe of CaM, we now have the necessary components to build a kinetic model of CDI in silico. We begin by first considering each lobe of CaM independently, using the experimental results obtained for CaM_{34} and CaM_{12} to optimize the model parameters. Because current LTCC models sufficiently address voltage-dependent activation and the voltage-dependent component of inactivation (VDI), we restrict our model to the context of CDI. Importantly, this focus does not ignore the importance of VDI, as this component can be added into any model owing to the independence of these two processes (Luo and Rudy, 1994; Jafri et al., 1998; Hirano and Hiraoka, 2003; Findlay et al., 2008), as such:

$$I(t) = I_{max}(t) * VDI(t) * CDI(t), \quad (5)$$

where $I(t)$ is the total current remaining after CDI and VDI are considered, and $I_{max}(t)$ is the maximum current amplitude based solely on channel activation and permeation. Thus, our CDI models are formulated to describe the time course of CDI after channels have fully activated.

To create kinetic models of CDI, we first considered the allosteric nature of this process (Faber et al., 2007; Mahajan et al., 2008). That is, fully activated channels bound to apoCaM open with a relatively high P_o (mode 1 gating), whereas channels harboring a Ca^{2+}-bound CaM transition into a low P_o mode of gating "mode Ca" (Imredy and Yue, 1994; Adams et al., 2014). Once in mode Ca, channels maintain the ability to open, but with a re-

Downloaded from http://rupress.org/jgp/article-pdf/150/12/1688/1798053/jgp_201812115.pdf by guest on 09 February 2026

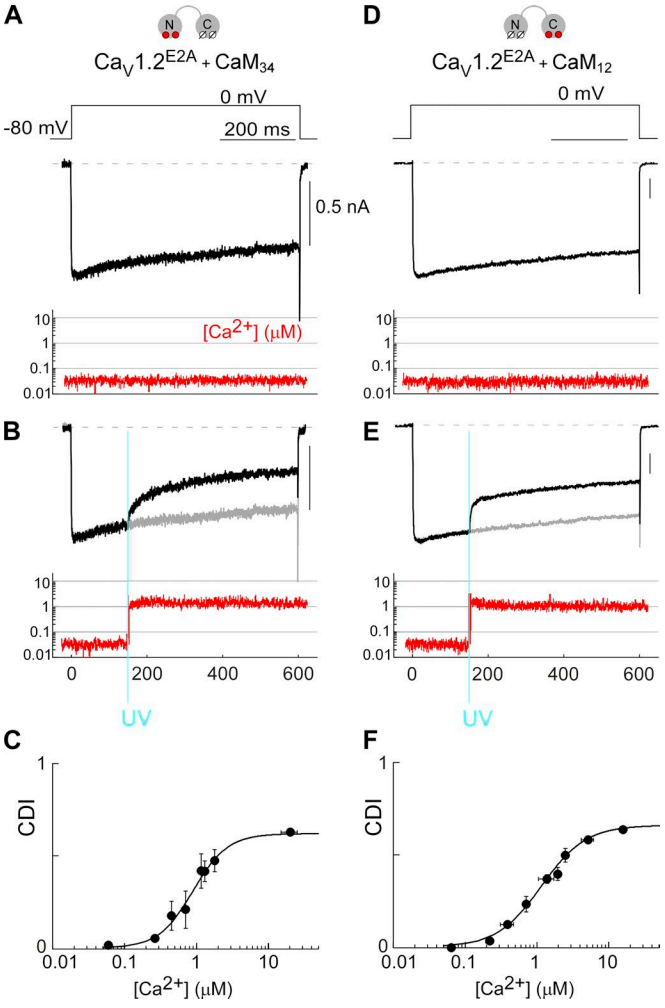

Figure 2. **Quantification of CaM lobe-specific CDI. (A–C)** $Ca_V1.2^{E2A}$ channels are coexpressed with mutant CaM_{34} in HEK293 cells, so as to characterize N-lobe CDI. **(A)** Li^+ currents before Ca^{2+} uncaging (black) with simultaneously measured resting $[Ca^{2+}]$ (red). **(B)** UV photo-uncaging of Ca^{2+} (blue) results in a step increase in $[Ca^{2+}]$ (red) and moderate reduction of Li^+ current (black) compared with preflash conditions (gray). **(C)** Steady-state N-lobe CDI as a function of $[Ca^{2+}]$, fitted with a Hill coefficient of 1.8 and K_d of 0.9 μM. Data are from 19 replicates (variable level UV flashes) across nine cells. Error bars indicate ±SEM. **(D–F)** CDI from $Ca_V1.2^{E2A}$ coexpressed with CaM_{12}. **(D)** Li^+ currents before Ca^{2+} uncaging (black) with simultaneously measured resting $[Ca^{2+}]$ (red). **(E)** UV photo-uncaging of Ca^{2+} (blue) results in a step increase in $[Ca^{2+}]$ (red) and moderate reduction of Li^+ current (black) compared with preflash conditions (gray). **(F)** Steady-state C-lobe CDI as a function of $[Ca^{2+}]$, fitted with a Hill coefficient of 1.4 and K_d of 1.15 μM. Data are from 21 replicates (variable level UV flashes) across 13 cells. Error bars indicate ±SEM.

duced open probability, resulting in CDI. Importantly, recent work indicates that the transition to mode Ca occurs upon the departure of apoCaM, such that channels devoid of apoCaM may be indistinguishable from channels bound to Ca^{2+}/CaM (Adams et al., 2014). We first applied these principles to create a model of N-lobe–mediated CDI. Here, we assume that the C-lobe will remain in the apo-state and thus will not contribute to CDI, whereas the N-lobe will independently orchestrate its own form of CDI (Fig. 2 C). We therefore created a four-state model of N-lobe CDI, such that each individual state represents a channel in either mode 1 (apoCaM bound, high P_o) or mode Ca (empty channel or Ca^{2+}/CaM bound, low P_o; Fig. 3 A). Thus, our model represents the minimal number of states required to reproduce CDI based on currently available structure–function data (Imredy and Yue, 1994; Tadross et al., 2008, 2010; Ben Johny et al., 2013; Adams et al., 2014). Specifically, state 1 represents apoCaM_{34} bound to the carboxy terminus of the channel. State 2 depicts a departure of the N-lobe from the channel, which then allows Ca^{2+} to bind transitioning to state 3. The calcified N-lobe can then subsequently bind to its effector site on the amino terminus of the channel, represented by state 4 (Dick et al., 2008; Tadross et al., 2008). For the binding of Ca^{2+} to CaM, we assumed simultaneous Ca^{2+} (un)binding, as has been demonstrated for the two EF hands within each lobe of CaM (Martin et al., 1985; Linse et al., 1991). Moreover, we define the open probability of state 1 (apoCaM_{34} bound) to be $P_{O,max}$ while assuming the open probabilities of states 2, 3, and 4 are reduced equally by a factor f_N (fractional open probability in mode Ca (Adams et al., 2014), such that

$$f_N = 1 - CDI_{max,N}, \tag{6}$$

and the open probability of each of these mode Ca states is $f_N{}^* P_{O,max}$. From our experimental measurements (Fig. 2 C), we obtain f_N = 0.38. We can then express the time-varying evolution of CDI as

$$CDI_N(t) = \frac{I_f(t)}{I_{nf}(t)} = \frac{}{M_{1,N}(t) + f_N{}^*[M_{2,N}(t) + M_{3,N}(t) + M_{4,N}(t)]}, \tag{7}$$

where $M_x(t)$ is the probability of channels being in state x at time t (see Supplementary text, Differential equations for N-lobe and C-lobe CDI, for detailed model equations). N-lobe states were defined as shown in Fig. 3 A, subject to the constraints as described in Supplementary text, Parameter constraints. Overall, the model contains six free parameters; however, constraints were placed on $k_{on,N}$ and $k_{off,N}$ based on prior experimental reports (Bayley et al., 1984; Martin et al., 1985; Stemmer and Klee, 1994; Black et al., 2005; Saucerman and Bers, 2008), leaving only four free parameters requiring full optimization (Supplementary text, Model setup and parameter optimization, and Parameter constraints).

We next optimized our model parameters (Table 1) to minimize the error between our model output and our kinetic (Fig. 2 B) and steady-state (Fig. 2 C) experimental data for CaM_{34}. To begin, we fitted our experimental Ca^{2+} measurements with a double exponential equation to provide a smooth Ca^{2+} input waveform for our model (Fig. 3 B, bottom; Supplementary text, Model setup and parameter optimization). Accordingly, we simulated currents in response to three different Ca^{2+} step inputs, yielding optimized rate constants as described in Table 1. Although these parameters do not definitively quantify all underlying aspects of the biological system, our model effectively recapitulates the kinetic and steady-state aspects of our experimental data (Figs. 3, B and C; red, simulation; black, experiment), with $k_{on,N}$ and $k_{off,N}$ comparable to experimentally measured values (Bayley et al., 1984; Martin et al., 1985; Stemmer and Klee, 1994; Black et al., 2005; Saucerman and Bers, 2008). Moreover, the parameters of this N-lobe–mediated CDI model are consistent with the known mechanisms of spatial Ca^{2+} selectivity of N-lobe CaM (Supplementary text, Parameter constraints; Dick et al., 2008; Tadross et al., 2008).

Downloaded from http://rupress.org/jgp/article-pdf/150/12/1688/1798053/jgp_201812115.pdf by guest on 09 February 2026

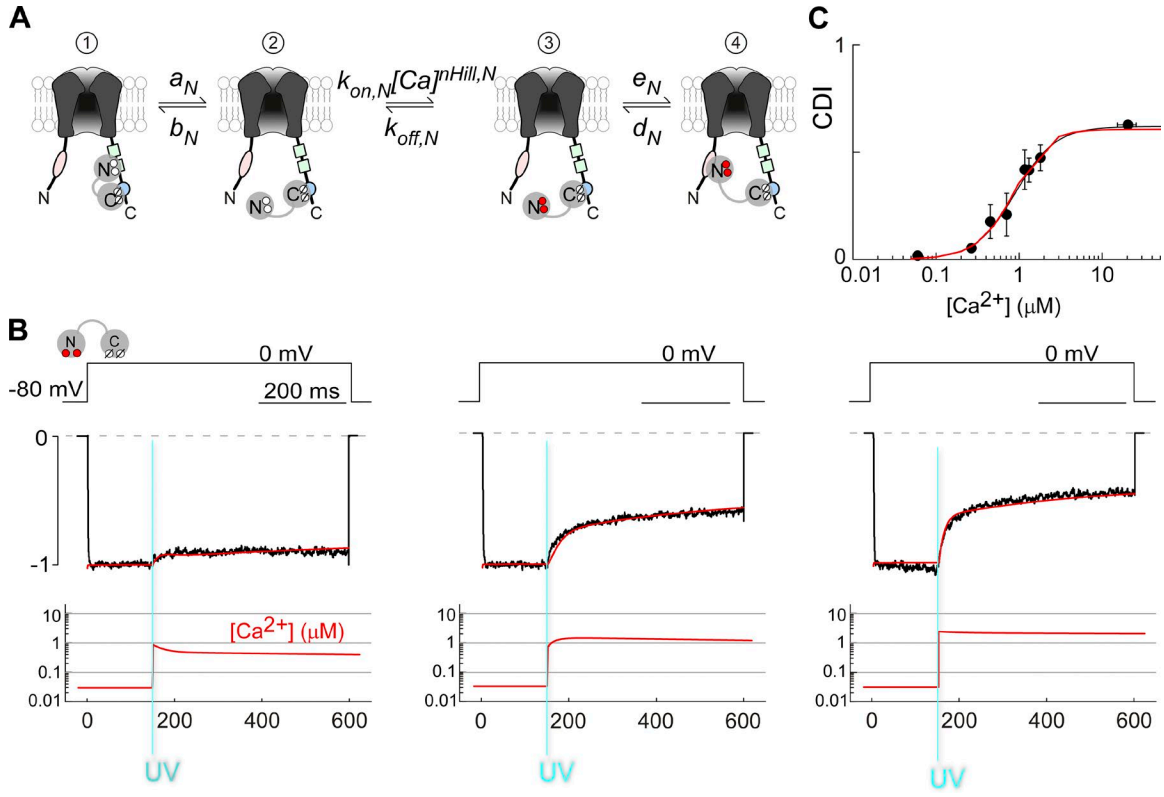

Figure 3. **Kinetic model of CDI mediated by N-lobe CaM. (A)** Schematic representation of N-lobe–mediated CDI model of $Ca_V1.2$ channels. Rate constants are shown above and below the arrows depicting the state transition (Table 1). **(B)** Simulated $I_{Ca(L)}$ (red) in response to three different levels of Ca^{2+} recapitulates the N-lobe CDI recorded from $Ca_V1.2^{E2A}$ coexpressed with CaM_{34} (black). Ca^{2+} step (red) is idealized (see text) from experimental data and used as the model input. **(C)** Steady-state N-lobe–mediated CDI predicted by this four-state N-lobe model (red) matches well to the experimental data (black, taken from Fig. 2 C as reference). Error bars indicate ±SEM.

Having established a functional model of N-lobe CaM signaling, we next sought to create a similar model for C-lobe–mediated CDI. Using the same approach as with the N-lobe model, we created a four-state model of C-lobe mediated CDI (Fig. 4 A, see Supplementary text, Differential equations for N-lobe and C-lobe CDI, for detailed differential equations for each mode). We again defined the open probability of state 1 ($apoCaM_{12}$ bound) to be $P_{O,max}$ while assuming the open probability of states 2, 3, and 4 to be $f_C * P_{O,max}$, with f_C defined as

$$f_C = 1 - CDI_{max,C}. \quad (8)$$

From our experimental measurements (Fig. 2 F), we obtain f_C = 0.34. We then express the time-varying extent of CDI as

$$CDI_C(t) = \frac{I_f(t)}{I_{nf}(t)} = M_{1,C}(t) + f_C * [M_{2,C}(t) + M_{3,C}(t) + M_{4,C}(t)], \quad (9)$$

where $M_x(t)$ is the probability of channels being in state x at time t (see Supplementary text, Differential equations for N-lobe and C-lobe CDI, for detailed model equations). We then optimized the free parameters (Table 1) fitting the model to the kinetic (Fig. 2 E) and steady-state (Fig. 2 F) experimental data for CaM_{12}. The simulated currents (Fig. 4 B) reproduce experimental results well, capturing the initial rapidly inactivating phase, the following slowly inactivating phase, and the steady-state response to Ca^{2+} (Fig. 4 C). Again, the kinetics of Ca^{2+} binding and unbinding to C-lobe of CaM, $k_{on,C}$ and $k_{off,C}$, are comparable to those experimentally described for this lobe (Bayley et al., 1984; Martin et al., 1985; Stemmer and Klee, 1994; Black et al., 2005; Saucerman and Bers, 2008). Moreover, the parameters of this C-lobe–mediated CDI model is consistent with the invariably local Ca^{2+} selectivity of C-lobe CaM (See Supplementary text, Parameter constraints, for details; Dick et al., 2008; Tadross et al., 2008).

Integrated model of CaM regulated CDI

Having established independent models of lobe-specific CaM-mediated CDI, we next sought to integrate these models into a full model representing the kinetic response of both lobes of CaM simultaneously (CaM_{WT}). Cognizant of the potential interdependence of the two lobes of CaM, we created a bilobal model of CDI consisting of 16 states which represent all possible combinations of the minimal four-state N- and C-lobe models (Fig. 5 A). Here, horizontal transitions represent C-lobe state changes, and vertical transitions represent N-lobe state changes. Our model incorporates the optimized rate constants from both the N- and C-lobe models (Figs. 3 A and 4 A and Table 1), as well as multiple cooperativity factors (g, h, k, l, m, n, p, and q) to account for potential communication between the lobes (Fig. 5 A). Consideration of thermodynamic microscopic reversibility reduces this to four free parameters (Table 1) as described in Supplementary Information, Differential equations for bilobal CDI and Parameter constraints. In addition, we assumed that a transiently dis-

Downloaded from http://rupress.org/jgp/article-pdf/150/12/1688/1798053/jgp_201812115.pdf by guest on 09 February 2026

Table 1. **Parameters used in CDI simulation**

Parameters	Values (units)
N-lobe–mediated CDI (CaM_{34})	
a_N	1.07×10^{-1} (ms^{-1})
b_N	2.46 (ms^{-1})
d_N	2.15×10^{-4} (ms^{-1})
e_N	5.44×10^{-3} (ms^{-1})
$k_{on,N}$	1.236×10^{5} ($mM^{-2} \cdot ms^{-1}$)
$k_{off,N}$	5.273×10^{-2} (ms^{-1})
$n_{Hill,N}$	1.8
f_N	0.38
C-lobe–mediated CDI (CaM_{12})	
a_C	14 (ms^{-1})
b_C	2.7×10^{3} (ms^{-1})
d_C	1.5×10^{-3} (ms^{-1})
e_C	3.5×10^{-3} (ms^{-1})
$k_{on,C}$	2.15×10^{4} ($mM^{-2} \cdot ms^{-1}$)
$k_{off,C}$	1.2×10^{-2} (ms^{-1})
$n_{Hill,C}$	1.4
f_C	0.34
Bilobal CDI (CaM_{WT})	
g	7.5
h	7.51×10^{-1}
n	2.656×10^{-2}
q	1.93×10^{3}
$m = g$	7.5
$p = g^*h$	5.63
$k = g^*n$	1.99×10^{-1}
$l = q^*h/n$	5.46×10^{4}
f_{WT}	0.12

sociated CaM (states 6, 7, 10, and 11) is unlikely to diffuse away from the channel alcove owing to the limiting rate of exchange between cytosolic and channel-associated CaMs (Chaudhuri et al., 2005). As in the reduced models, the open probability in state 1 (both lobes of apoCaM bound) is defined to be $P_{O,max}$; the open probability in states 2, 3, and 4 is defined as $f_N * P_{O,max}$; the open probability in states 5, 9, and 13 is $f_C * P_{O,max}$; and the open probability in states 6, 7, 8, 10, 11, 12, 14, 15, and 16 is $f_{WT} * P_{O,max}$, where $f_{WT} = 1 - CDI_{max} = 0.12$ (Fig. 1 H) and CDI is defined as:

$$CDI\left(t\right) = \frac{I_f(t)}{I_{nf}(t)} = \frac{M_1(t) + f_N^*[M_2(t) + M_3(t) + M_4(t)] + f_C^*[M_5(t) + M_9(t) + M_{13}(t)] + f_{WT}^*\begin{bmatrix} M_6(t) + M_7(t) + M_8(t) + M_{10}(t) + M_{11}(t) + \\ M_{12}(t) + M_{14}(t) + M_{15}(t) + M_{16}(t) \end{bmatrix}}{} \quad (10)$$

where $M_x(t)$ is the probability of channels being in state x at time t (see detailed model equations in Supplementary text, Differential equations for bilobal CDI).

Fitting this model to our experimental data for $Ca_V1.2^{E2A}$ co-expressed with CaM_{WT} enabled us to optimize the parameters (Table 1, Supplementary text, Differential equations for bilobal CDI and Parameter constraints), resulting in a bilobal model that approximates both the kinetic (Fig. 5 B) and steady-state (Fig. 5 C) behavior of CaM-mediated CDI. In addition, the model predicts cooperativity factors with both positive (>1, increased likelihood of the transition) and negative (<1, decreased likelihood of the transition) cooperativity. Importantly, setting all cooperativity factors to unity (no cooperativity) results in a model that fails to reproduce the experimental data (Supplementary text, The importance of cooperativity factors). Therefore, although these cooperativity factors may not quantify the precise physiological mechanism, some form of cooperativity is likely to exist. Thus, our model explicitly captures the mechanistic interplay between the two lobes of CaM, an important feature of CDI not found in previous models.

Modeling calmodulinopathy

To gauge the ability of our bilobal CDI model to make predictions under pathophysiological conditions, we applied it in the context of a known calmodulinopathic mutation D130G. This missense mutation occurs within the fourth EF hand of CaM, resulting a ∼50-fold decrease in the Ca^{2+} binding affinity of the C-lobe (Crotti et al., 2013; Hwang et al., 2014) and results in a significantly increased QT interval, rendering patients susceptible to arrhythmias (Arevalo et al., 2007). At the cellular level, this is demonstrated by a prolongation of the action potential (Fig. 6 A), which is largely caused by disruption of $Ca_V1.2$ CDI (Limpitikul et al., 2014). We thus applied our 16-state model to CaM_{D130G}-mediated CDI. To begin, we experimentally probed CDI from $Ca_V1.2$ channels that coexpressed CaM_{D130G} using our photo-uncaging technique (Fig. 6, B and C, black). Here, the CDI is significantly reduced even at very high concentrations of Ca^{2+} (Fig. 6 C). Moreover, the steady-state CDI mediated by CaM_{D130G} (Fig. 6 C) can be fitted with a Hill equation (Eq. 4) with $CDI_{max,D130G} = 0.62$, $nHill_{D130G} = 1.8$, and $K_{d,D130G} = 0.9$ µM ($R^2 = 0.98$). Notably, this represents the identical parameters used to describe the steady-state behavior of N-lobe–mediated CDI. Thus, this mutation in a single EF hand appears to disrupt CDI to the same extent as CaM_{34}, in which both C-lobe EF hands are ablated.

To simulate this mutation with our 16-state CDI model, we decreased $k_{on,C}$ by 50-fold to account for the loss of Ca^{2+} binding affinity for this lobe and dramatically reduced the cooperativity factors g and m, preventing CDI from proceeding via C-lobe CaM (Table 2). The resultant model was able to predict the kinetic (Fig. 6 B) and steady-state (Fig. 6 C) properties of CaM_{D130G}-mediated CDI, thus demonstrating the utility of this bilobal CDI model in both physiological and pathological conditions.

Discussion

CDI is a critical regulatory feature of $Ca_V1.2$ channels, playing a pivotal role in setting the action potential duration in the heart. Although multiple cardiac and neuronal models use CDI components (Hund and Rudy, 2004; ten Tusscher et al., 2004; Faber et al., 2007; Mahajan et al., 2008), few take into account the detailed

Downloaded from http://rupress.org/jgp/article-pdf/150/12/1688/1798053/jgp_201812115.pdf by guest on 09 February 2026

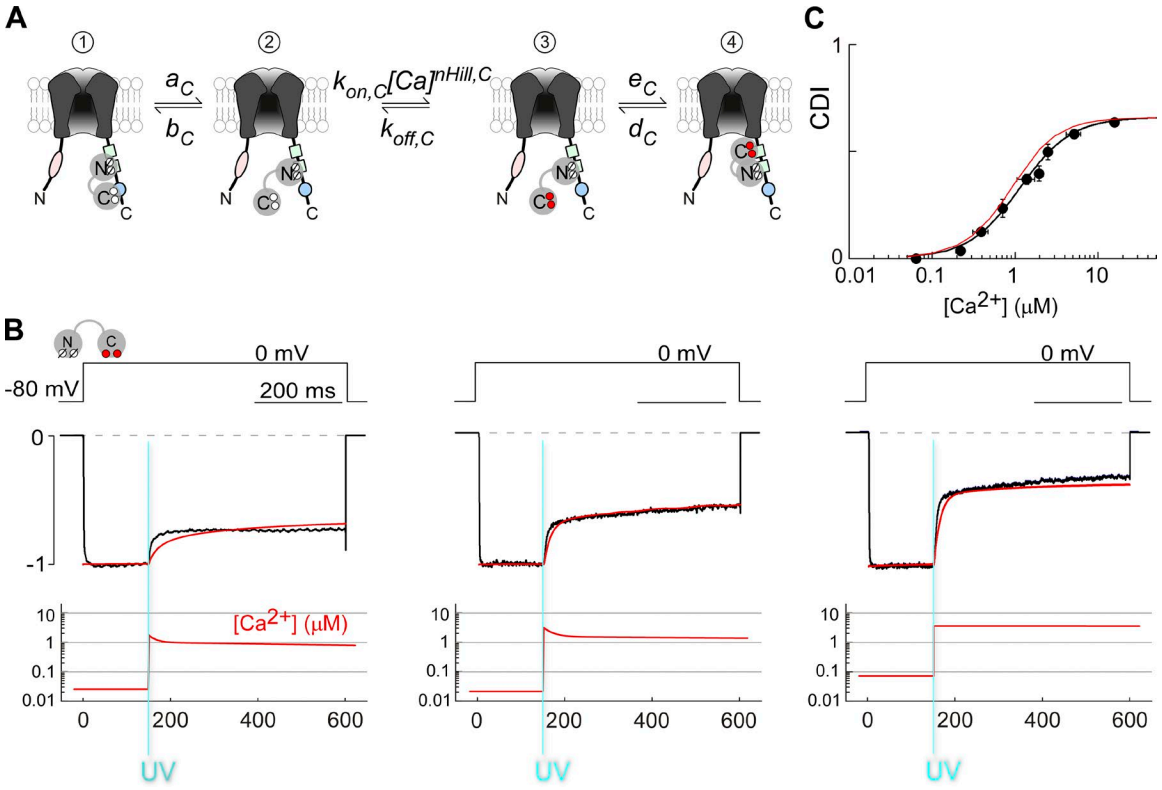

Figure 4. **Kinetic model of CDI mediated by C-lobe CaM. (A)** Schematic representation of C-lobe–mediated CDI model of $Ca_V1.2$ channels. Rate constants are shown above and below the arrows depicting state transitions (Table 1). **(B)** Simulated $I_{Ca(L)}$ (red) in response to three different levels of Ca^{2+} recapitulates the C-lobe CDI recorded from $Ca_V1.2^{E2A}$ coexpressed with CaM_{12} (black). Ca^{2+} step (red) is idealized (see text) from experimental data and used as the model input. **(C)** Steady-state C-lobe–mediated CDI predicted by this four-state C-lobe model (red) matches well to the experimental data (black, taken from Fig. 2 F as reference).

kinetics or bilobal nature of CaM binding to the channel. Here, we obtain rigorous experimental data and use it to create a detailed kinetic model of $Ca_V1.2$ CDI featuring full bilobal CaM regulation. Specifically, we measured the kinetic response of channel inactivation caused by measurable changes in intracellular Ca^{2+} by pairing photo-uncaging with simultaneous patch clamp recording (Tadross et al., 2013; Lee et al., 2015; Dick et al., 2016). This method allowed us to uncouple channel gating from intracellular Ca^{2+} dynamics, enabling precise control of bulk cytosolic Ca^{2+} and overcoming the ambiguity caused by diffusion-limited Ca^{2+} dispersion in traditional patch-clamp experiments. Moreover, by using single and combinations of Ca^{2+}-sensitive dyes with different affinities, we were able to accurately measure $[Ca^{2+}]$ across a wide range of values from resting (~0.1 μM) to locally elevated (as high as 100 μM at the mouth of the channel; Neher, 1998). As such, we concurrently measured CDI in response to known concentrations of Ca^{2+}. This use of high-resolution data enabled the development of two independent single-lobe models of $Ca_V1.2$ CDI and a 16-state bilobal model of CDI.

To build this bilobal model of CDI, we used a reductionist approach, first examining the CDI elicited by each lobe of CaM independently. Our experimental data showed that despite minimal difference in steady-state CDI profiles, N-lobe-mediated CDI exhibits much slower kinetics compared with C-lobe-mediated CDI. Using this data, we created a minimal four-state single-lobe model for each lobe of CaM and incorporated these two models into a 16-state bilobal model of CDI, enabling us to gauge the cooperativity between the two lobes in the context of $Ca_V1.2$ binding. Although cooperativity between the N- and C-lobe of CaM is well known in response to Ca^{2+} binding (Teleman et al., 1986; Yazawa et al., 1987; Jaren et al., 2002), the extent of cooperativity in the initiation of $Ca_V1.2$ CDI remains undetermined. Given the importance of this feature, we can corroborate the positive cooperativity factor implied by our model by scrutinizing our experimental data. Specifically, we express the closed-form solution of steady-state bilobal mediated CDI as

$$CDI(\infty) = \frac{\left[\begin{array}{c} K_C{}^{*}Ca^{nHill,C}{}^{*}(1-P_C) + K_N{}^{*}Ca^{nHill,N}{}^{*}(1-P_N) \\ + K_C{}^{*}K_N{}^{*}\lambda{}^{*}Ca^{nHill,WT}{}^{*}(1-P_{WT}) \end{array}\right]}{\left[1 + K_C{}^{*}Ca^{nHill,C} + K_N{}^{*}Ca^{nHill,N} + K_C{}^{*}K_N{}^{*}\lambda{}^{*}Ca^{nHill,WT}\right]}, \quad (11)$$

where K_N and K_C are the K_d of N- and C-lobe CaM respectively; P_N, P_C, and P_{WT} are the relative open probabilities of mode Ca compared with mode 1 for N-, C-, and both lobes of CaM, respectively; and λ is the cooperativity factor (see Supplementary text, Derivation of cooperativity between CaM lobes, for derivation). Here, λ >1 and λ < 1 represent positive and negative cooperativity between CaM lobes, respectively. Applying this equation to our steady-state CaM_{WT} CDI data (Fig. 1 H) reveals λ = ~5, demonstrating that both lobes of CaM modulate $Ca_V1.2$ in an interdependent manner with positive cooperativity, which implies that independent four-state N- and C-lobe models might not be sufficient to correctly describe the kinetics of the bilobal CDI process.

Downloaded from http://rupress.org/jgp/article-pdf/150/12/1688/1798053/jgp_201812115.pdf by guest on 09 February 2026

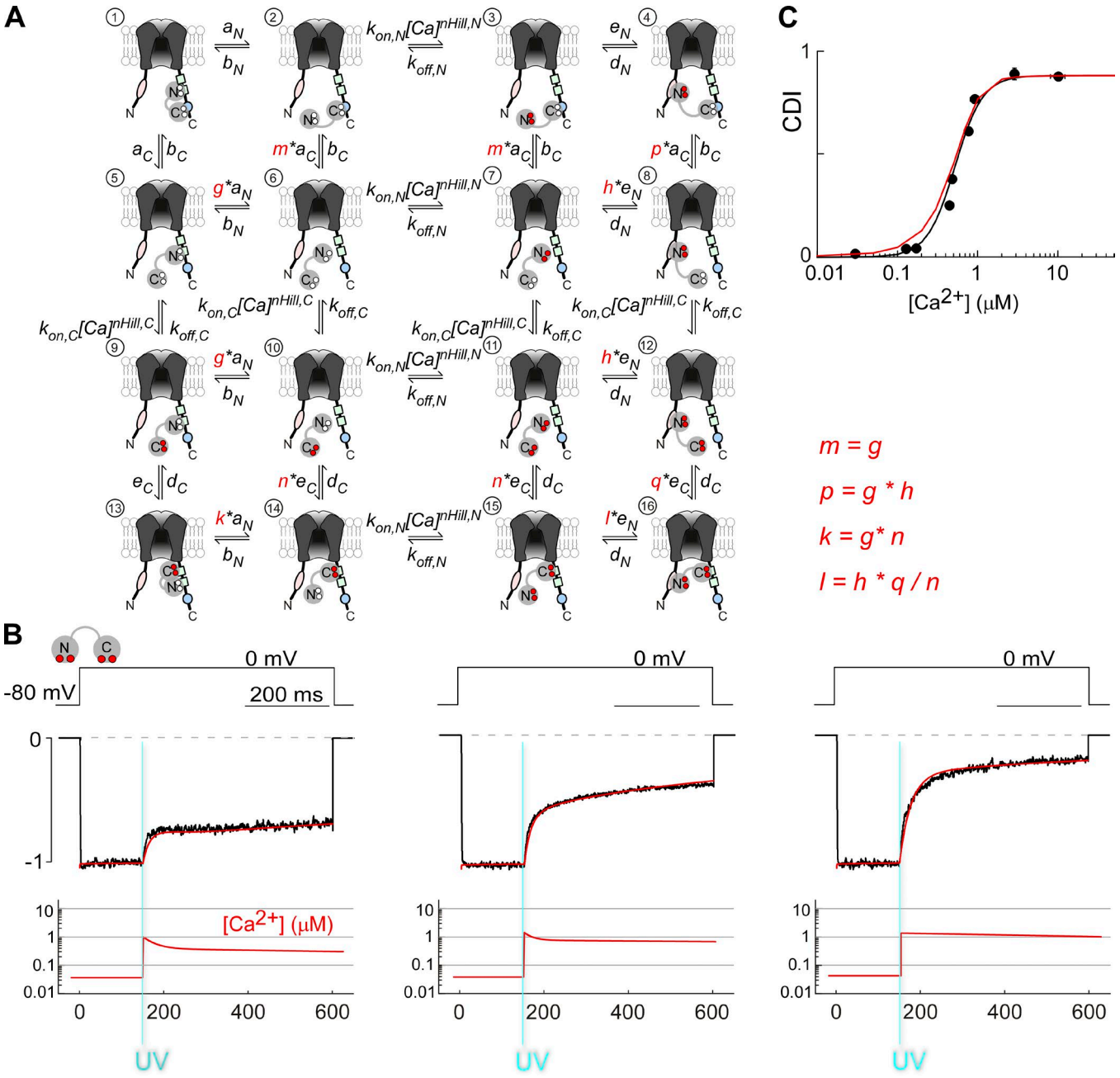

Figure 5. **Full bilobal model of CDI. (A)** Schematic representation of 16-state CaM-mediated $Ca_V1.2$ CDI. Rate constants are shown above and below the arrows depicting the state transition (Table 1). **(B)** Simulated $I_{Ca(L)}$ (red) in response to three different levels of Ca^{2+} recapitulates the CDI recorded from $Ca_V1.2^{E2A}$ coexpressed with CaM_{WT} (black). Ca^{2+} step (red) is idealized (see text) from experimental data and used as the model input. **(C)** Steady-state CaM-mediated $Ca_V1.2$ CDI predicted by this 16-state bilobal model (red) matches well to the experimental data (black, taken from Fig. 1 H as reference). Error bars indicate ±SEM.

Moreover, cooperativity implies that perturbation in one lobe of CaM can affect overall CDI to a larger extent than would be predicted in a model in which each lobe acts independently and may be an important feature in understanding the pathogenesis of diseases such as calmodulinopathies.

We therefore applied our bilobal CDI model to simulate the effect of the LQTS-associated calmodulinopathy mutation, D130G (Crotti et al., 2013; Limpitikul et al., 2014, 2017; Yin et al., 2014). Residing in the fourth EF hand of CaM, this mutation minimally increases the apoCaM binding affinity to $Ca_V1.2$ (approximately two-fold; Limpitikul et al., 2014) while dramatically diminishing the Ca^{2+} binding affinity of C-lobe CaM (~50-fold; Crotti et al., 2013; Hwang et al., 2014), with no discernable effect on the Ca^{2+} binding affinity of N-lobe CaM (Hwang et al., 2014). Interestingly, although the C-lobe of CaM_{D130G} maintains some Ca^{2+}-binding capacity, our experimental data show that overall, CaM_{D130G} behaves nearly identically to CaM_{34} (Figs. 2 C and 6 C). Moreover, prediction from our bilobal CDI model corroborates this finding. Upon decreasing $k_{on,C}$ by 50-fold and dramatically reducing the cooperativity factors g and m (thus preventing CDI from proceeding via C-lobe CaM), the model accurately recapitulates both the kinetic and steady-state behavior of CaM_{D130G}. If

Downloaded from http://rupress.org/jgp/article-pdf/150/12/1688/1798053/jgp_201812115.pdf by guest on 09 February 2026

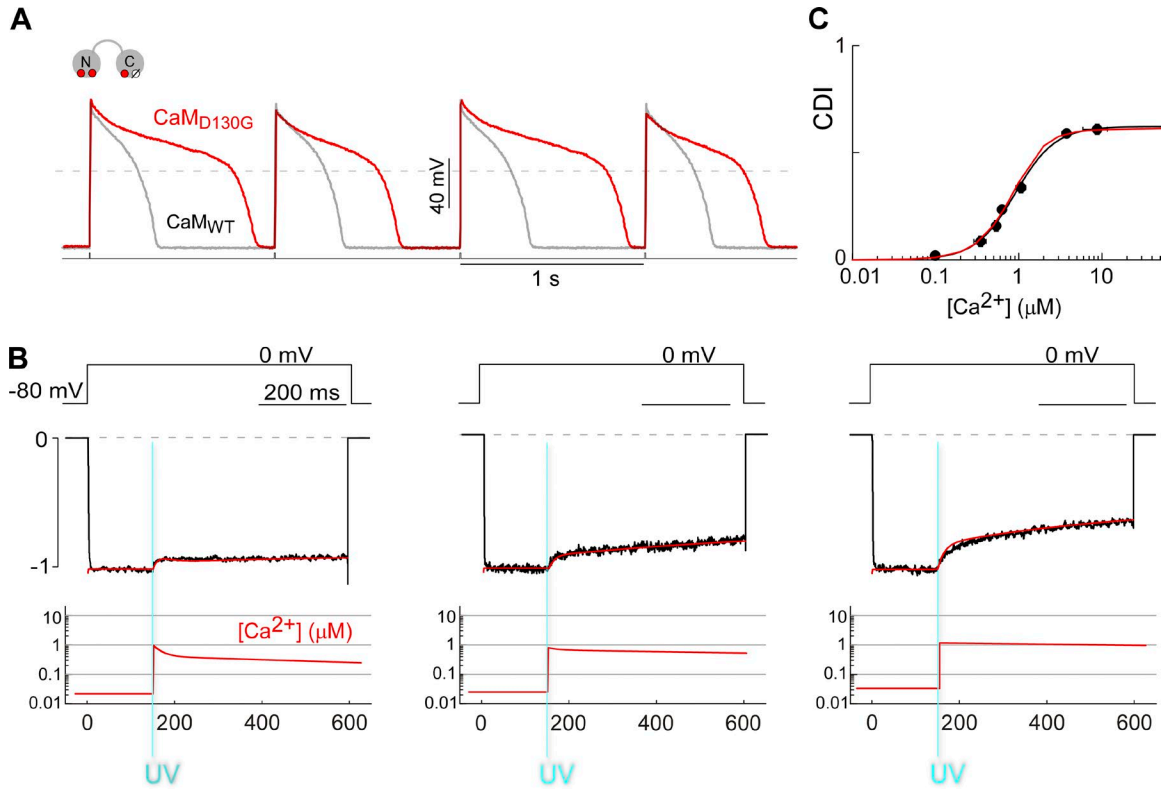

Figure 6. **Full bilobal model of CDI in the context of a calmodulinopathic mutation. (A)** Disruption of action potentials in guinea pig ventricular myocytes by CaM_{D130G}. When CaM_{D130G} was overexpressed, cardiac action potentials become markedly lengthened and irregular (red) compared with CaM_{WT} (shown in gray). Adapted from Limpitikul et al. (2014). **(B)** Simulated $I_{Ca(L)}$ (red) in response to three different levels of Ca^{2+} recapitulates the CDI recorded from $Ca_V1.2^{E2A}$ coexpressed with CaM_{D130G} (black). Ca^{2+} step (red) is idealized (see text) from experimental data and used as the model input. **(C)** Steady-state CaM-mediated $Ca_V1.2$ CDI predicted by the adjusted 16-state bilobal model (red) matches well to the experimental data (black). Data are from 18 replicates across eight cells. Error bars indicate ±SEM.

strong interlobal cooperativity could be verified experimentally, it would imply that when the Ca^{2+}-binding affinity of one lobe of CaM falls under a certain threshold, CDI mediated by that lobe may become physiologically ineffective. In fact, experimental data shows that even a fivefold reduction in the C-lobe Ca^{2+} binding affinity (F142L mutation; Crotti et al., 2013; Hwang et al., 2014) can alter the overall behavior of CaM to resemble that of CaM_{34} (Limpitikul et al., 2014).

Although our models can approximate the kinetics of CDI in both physiological and pathological conditions relatively well, there exist experimental and computational limitations. For example, rate constants for the CDI models were optimized using data obtained at room temperature, which are likely slower than those at a physiological 37°C. However, with known temperature coefficient (Q_{10}), rate constants at 37°C can be extrapolated (Faber et al., 2007; Mahajan et al., 2008). In addition, here, $Ca_V1.2$ channels and CaM variants were heterologously expressed in HEK293 cells, which lack some modulatory mechanisms inherent to cardiomyocytes, such as adrenergic regulation of $Ca_V1.2$ (Miriyala et al., 2008). Although we were not able to incorporate all regulatory feedbacks of $Ca_V1.2$, this reductionist approach could be advantageous in that it allows the CDI module to be incorporated into models of different cell types. In addition, little is known about the conformational changes that result in CDI and thus cannot be explicitly included in the model. Moreover, we used the assumption that states 2 and 3 will have a low open probability based on the lack of apoCaM binding; however, it must be noted that this hypothesis is based on the work of Adams et al. (2014) and remains to be fully verified. Furthermore, consideration of the sensitivity of the model to each parameter (Supplementary text, Parameter sensitivity) reveals that the final parameter set does not comprise a unique solution to the system. Although the majority of the parameters correspond to a well-defined minimum of the cost function, a few are associated with a plateau at the minimum error value (see Supplementary text, Parameter sensitivity, for details). This is not surprising or uncommon behavior in biological dynamical systems, as they may often be decomposed into fast and slow subsystems. In such cases, when a parameter that governs kinetics of the fast subsystem is made sufficiently large, a wide range of parameter values will yield similar dynamical behavior. This behavior indicates that there is a threshold value at which the kinetics of the fast subsystem controlled by this parameter effectively becomes instantaneous from the temporal perspective of the slower subsystems, which are rate limiting. Such robustness to parameter variation is not uncommon in biological systems. Thus, the final parameter values of the model presented here are not necessarily intended to quantitatively capture and reproduce the kinetic features of all the underlying biophysical processes associated with each gating transition of the channel protein, but rather as appropriate

Downloaded from http://rupress.org/jgp/article-pdf/150/12/1688/1798053/jgp_201812115.pdf by guest on 09 February 2026

Table 2. **Parameter for long-QT CaM (CaM_{D130G}) simulation**

Parameter	Values (units)
a_N'	Unchanged
b_N'	Unchanged
d_N'	Unchanged
e_N'	Unchanged
$k_{on,N}'$	Unchanged
$k_{off,N}'$	Unchanged
$n_{Hill,N}'$	Unchanged
f_N'	Unchanged
a_C'	Unchanged
b_C'	Unchanged
d_C'	Unchanged
e_C'	Unchanged
$k_{on,C}'$	4.3×10^2 ($mM^{-2} \cdot ms^{-1}$)
$k_{off,C}'$	Unchanged
$n_{Hill,C}'$	Unchanged
f_C'	Unchanged
g'	7.5×10^{-4}
h'	Unchanged
n'	Unchanged
q'	Unchanged
f_{WT}'	Unchanged

values representing a simplified mechanistic model system capable of reproducing experimentally observed channel behavior. Finally, a few commonly used LTCC models do not assume independence between channel activation and CDI (Greenstein and Winslow, 2002; Faber et al., 2007; Miriyala et al., 2008; Decker et al., 2009). Thus, integrating our CDI formulations into these LTCC models may be nontrivial in that the combined models would require a large number of states (~80 with a five-state activation model). However, the model size is not a limitation for stochastic gating simulations, and methods for handling such models in ODE-based simulations have been established previously (Greenstein et al., 2006).

Overall, beyond predicting the CDI profile of LQTS-associated calmodulinopathies, our model could be applied in a broader context to gain insights into the (patho)physiology of cardiac electrical activity. Previous studies have implied that CDI, compared with VDI, may be the dominant form of feedback regulation of $Ca_V1.2$ in the context of the cardiac action potential (Sun et al., 1997; Morotti et al., 2012) and the development of arrhythmia (Tanskanen et al., 2005; Morotti et al., 2012). Therefore, it is critical to use a realistic mathematical representation of CDI that can capture the distinct kinetics and cooperativity of the two lobes of CaM. Built from experimentally derived knowledge of fundamental biophysical gating mechanisms, this bilobal kinetic model of CDI can be used in cell and tissue scale models to make reliable predictions about cardiac electrical activity. Finally, the model can be used within other cellular contexts, including neurons, vascular and gastrointestinal smooth muscles, and chromaffin cells (Zamponi et al., 2015). Therefore, this bilobal CDI model could be an invaluable asset to the field of computational electrophysiology.

Acknowledgments

David T. Yue, who originally conceptualized this work, passed away on December 23, 2014. His mentorship, wisdom, and kindness are greatly missed. We thank Dr. Shin Rong Lee for advice and training with the photolysis system and thank Wanjun Yang for dedicated technical support. We also thank Dr. Gordon Tomaselli for providing valuable advice and discussions, and Dr. Manu Ben-Johny and members of the Calcium Signals Lab for ongoing feedback and support.

This work was supported by grants: American Heart Association Pre-doctoral Fellowship (W.B. Limpitikul) and National Institutes of Health R01HL105239 (J.L. Greenstein and R.L. Winslow) and R01MH065531 (W.B. Limpitikul, D.T. Yue, and I.E. Dick).

The authors declare no competing financial interests.

Author contributions: W.B. Limpitikul collected and analyzed data and wrote and edited the manuscript. J.L. Greenstein, R.L. Winslow, and I.E. Dick supervised the overall project and wrote and edited the manucript. D.T. Yue originally envisioned and conceptualized this work.

Richard W. Aldrich served as editor.

Submitted: 7 May 2018
Revised: 1 August 2018
Accepted: 26 October 2018

References

Adams, P.J., M. Ben-Johny, I.E. Dick, T. Inoue, and D.T. Yue. 2014. Apocalmodulin itself promotes ion channel opening and Ca(2+) regulation. *Cell.* 159:608–622. https://doi.org/10.1016/j.cell.2014.09.047

Arevalo, H., B. Rodriguez, and N. Trayanova. 2007. Arrhythmogenesis in the heart: Multiscale modeling of the effects of defibrillation shocks and the role of electrophysiological heterogeneity. *Chaos.* 17:015103. https://doi.org/10.1063/1.2430637

Bayley, P., P. Ahlström, S.R. Martin, and S. Forsen. 1984. The kinetics of calcium binding to calmodulin: Quin 2 and ANS stopped-flow fluorescence studies. *Biochem. Biophys. Res. Commun.* 120:185–191. https://doi.org/10.1016/0006-291X(84)91431-1

Ben Johny, M., P.S. Yang, H. Bazzazi, and D.T. Yue. 2013. Dynamic switching of calmodulin interactions underlies Ca2+ regulation of CaV1.3 channels. *Nat. Commun.* 4:1717. https://doi.org/10.1038/ncomms2727

Black, D.J., D.B. Halling, D.V. Mandich, S.E. Pedersen, R.A. Altschuld, and S.L. Hamilton. 2005. Calmodulin interactions with IQ peptides from voltage-dependent calcium channels. *Am. J. Physiol. Cell Physiol.* 288:C669–C676. https://doi.org/10.1152/ajpcell.00191.2004

Bodi, I., G. Mikala, S.E. Koch, S.A. Akhter, and A. Schwartz. 2005. The L-type calcium channel in the heart: the beat goes on. *J. Clin. Invest.* 115:3306–3317. https://doi.org/10.1172/JCI27167

Chaudhuri, D., B.A. Alseikhan, S.Y. Chang, T.W. Soong, and D.T. Yue. 2005. Developmental activation of calmodulin-dependent facilitation of cerebellar P-type Ca2+ current. *J. Neurosci.* 25:8282–8294. https://doi.org/10.1523/JNEUROSCI.2253-05.2005

Crotti, L., C.N. Johnson, E. Graf, G.M. De Ferrari, B.F. Cuneo, M. Ovadia, J. Papagiannis, M.D. Feldkamp, S.G. Rathi, J.D. Kunic, et al. 2013. Calmodulin mutations associated with recurrent cardiac arrest in infants. *Circulation.* 127:1009–1017. https://doi.org/10.1161/CIRCULATIONAHA.112.001216

Downloaded from http://rupress.org/jgp/article-pdf/150/12/1688/1798053/jgp_201812115.pdf by guest on 09 February 2026

Dafi, O., L. Berrou, Y. Dodier, A. Raybaud, R. Sauvé, and L. Parent. 2004. Negatively charged residues in the N-terminal of the AID helix confer slow voltage dependent inactivation gating to CaV1.2. *Biophys. J.* 87:3181–3192. https://doi.org/10.1529/biophysj.104.045559

Decker, K.F., J. Heijman, J.R. Silva, T.J. Hund, and Y. Rudy. 2009. Properties and ionic mechanisms of action potential adaptation, restitution, and accommodation in canine epicardium. *Am. J. Physiol. Heart Circ. Physiol.* 296:H1017–H1026. https://doi.org/10.1152/ajpheart.01216.2008

Dick, I.E., M.R. Tadross, H. Liang, L.H. Tay, W. Yang, and D.T. Yue. 2008. A modular switch for spatial Ca2+ selectivity in the calmodulin regulation of CaV channels. *Nature.* 451:830–834. https://doi.org/10.1038/nature06529

Dick, I.E., R. Joshi-Mukherjee, W. Yang, and D.T. Yue. 2016. Arrhythmogenesis in Timothy Syndrome is associated with defects in Ca(2+)-dependent inactivation. *Nat. Commun.* 7:10370. https://doi.org/10.1038/ncomms10370

Ellinor, P.T., J. Yang, W.A. Sather, J.F. Zhang, and R.W. Tsien. 1995. Ca2+ channel selectivity at a single locus for high-affinity Ca2+ interactions. *Neuron.* 15:1121–1132. https://doi.org/10.1016/0896-6273(95)90100-0

Erickson, M.G., B.A. Alseikhan, B.Z. Peterson, and D.T. Yue. 2001. Preassociation of calmodulin with voltage-gated Ca(2+) channels revealed by FRET in single living cells. *Neuron.* 31:973–985. https://doi.org/10.1016/S0896-6273(01)00438-X

Faber, G.M., J. Silva, L. Livshitz, and Y. Rudy. 2007. Kinetic properties of the cardiac L-type Ca2+ channel and its role in myocyte electrophysiology: a theoretical investigation. *Biophys. J.* 92:1522–1543. https://doi.org/10.1529/biophysj.106.088807

Findlay, I., S. Suzuki, S. Murakami, and Y. Kurachi. 2008. Physiological modulation of voltage-dependent inactivation in the cardiac muscle L-type calcium channel: a modelling study. *Prog. Biophys. Mol. Biol.* 96:482–498. https://doi.org/10.1016/j.pbiomolbio.2007.07.002

Greenstein, J.L., and R.L. Winslow. 2002. An integrative model of the cardiac ventricular myocyte incorporating local control of Ca2+ release. *Biophys. J.* 83:2918–2945. https://doi.org/10.1016/S0006-3495(02)75301-0

Greenstein, J.L., R. Hinch, and R.L. Winslow. 2006. Mechanisms of excitation-contraction coupling in an integrative model of the cardiac ventricular myocyte. *Biophys. J.* 90:77–91. https://doi.org/10.1529/biophysj.105.065169

Hirano, Y., and M. Hiraoka. 2003. Ca2+ entry-dependent inactivation of L-type Ca current: a novel formulation for cardiac action potential models. *Biophys. J.* 84:696–708. https://doi.org/10.1016/S0006-3495(03)74889-9

Hund, T.J., and Y. Rudy. 2004. Rate dependence and regulation of action potential and calcium transient in a canine cardiac ventricular cell model. *Circulation.* 110:3168–3174. https://doi.org/10.1161/01.CIR.0000147231.69595.D3

Hwang, H.S., F.R. Nitu, Y. Yang, K. Walweel, L. Pereira, C.N. Johnson, M. Faggioni, W.J. Chazin, D. Laver, A.L. George Jr., et al. 2014. Divergent regulation of ryanodine receptor 2 calcium release channels by arrhythmogenic human calmodulin missense mutants. *Circ. Res.* 114:1114–1124. https://doi.org/10.1161/CIRCRESAHA.114.303391

Ikeda, S., A. He, S.W. Kong, J. Lu, R. Bejar, N. Bodyak, K.H. Lee, Q. Ma, P.M. Kang, T.R. Golub, and W.T. Pu. 2009. MicroRNA-1 negatively regulates expression of the hypertrophy-associated calmodulin and Mef2a genes. *Mol. Cell. Biol.* 29:2193–2204. https://doi.org/10.1128/MCB.01222-08

Imredy, J.P., and D.T. Yue. 1994. Mechanism of Ca(2+)-sensitive inactivation of L-type Ca2+ channels. *Neuron.* 12:1301–1318. https://doi.org/10.1016/0896-6273(94)90446-4

Jafri, M.S., J.J. Rice, and R.L. Winslow. 1998. Cardiac Ca2+ dynamics: the roles of ryanodine receptor adaptation and sarcoplasmic reticulum load. *Biophys. J.* 74:1149–1168. https://doi.org/10.1016/S0006-3495(98)77832-4

Jaren, O.R., J.K. Kranz, B.R. Sorensen, A.J. Wand, and M.A. Shea. 2002. Calcium-induced conformational switching of Paramecium calmodulin provides evidence for domain coupling. *Biochemistry.* 41:14158–14166. https://doi.org/10.1021/bi026340+

Keen, J.E., R. Khawaled, D.L. Farrens, T. Neelands, A. Rivard, C.T. Bond, A. Janowsky, B. Fakler, J.P. Adelman, and J. Maylie. 1999. Domains responsible for constitutive and Ca(2+)-dependent interactions between calmodulin and small conductance Ca(2+)-activated potassium channels. *J. Neurosci.* 19:8830–8838. https://doi.org/10.1523/JNEUROSCI.19-20-08830.1999

Lee, S.R., P.J. Adams, and D.T. Yue. 2015. Large Ca^{2+}-dependent facilitation of Ca(V)2.1 channels revealed by Ca^{2+} photo-uncaging. *J. Physiol.* 593:2753–2778. https://doi.org/10.1113/JP270091

Limpitikul, W.B., I.E. Dick, R. Joshi-Mukherjee, M.T. Overgaard, A.L. George Jr., and D.T. Yue. 2014. Calmodulin mutations associated with long QT syndrome prevent inactivation of cardiac L-type Ca(2+) currents and promote proarrhythmic behavior in ventricular myocytes. *J. Mol. Cell. Cardiol.* 74:115–124. https://doi.org/10.1016/j.yjmcc.2014.04.022

Limpitikul, W.B., I.E. Dick, D.J. Tester, N.J. Boczek, P. Limphong, W. Yang, M.H. Choi, J. Babich, D. DiSilvestre, R.J. Kanter, et al. 2017. A Precision Medicine Approach to the Rescue of Function on Malignant Calmodulinopathic Long-QT Syndrome. *Circ. Res.* 120:39–48. https://doi.org/10.1161/CIRCRESAHA.116.309283

Linse, S., A. Helmersson, and S. Forsén. 1991. Calcium binding to calmodulin and its globular domains. *J. Biol. Chem.* 266:8050–8054.

Lipp, P., C. Lüscher, and E. Niggli. 1996. Photolysis of caged compounds characterized by ratiometric confocal microscopy: a new approach to homogeneously control and measure the calcium concentration in cardiac myocytes. *Cell Calcium.* 19:255–266. https://doi.org/10.1016/S0143-4160(96)90026-3

Luo, C.H., and Y. Rudy. 1994. A dynamic model of the cardiac ventricular action potential. I. Simulations of ionic currents and concentration changes. *Circ. Res.* 74:1071–1096. https://doi.org/10.1161/01.RES.74.6.1071

Mahajan, A., Y. Shiferaw, D. Sato, A. Baher, R. Olcese, L.H. Xie, M.J. Yang, P.S. Chen, J.G. Restrepo, A. Karma, et al. 2008. A rabbit ventricular action potential model replicating cardiac dynamics at rapid heart rates. *Biophys. J.* 94:392–410. https://doi.org/10.1529/biophysj.106.98160

Martin, S.R., A. Andersson Teleman, P.M. Bayley, T. Drakenberg, and S. Forsen. 1985. Kinetics of calcium dissociation from calmodulin and its tryptic fragments. A stopped-flow fluorescence study using Quin 2 reveals a two-domain structure. *Eur. J. Biochem.* 151:543–550. https://doi.org/10.1111/j.1432-1033.1985.tb09137.x

Miriyala, J., T. Nguyen, D.T. Yue, and H.M. Colecraft. 2008. Role of CaVbeta subunits, and lack of functional reserve, in protein kinase A modulation of cardiac CaV1.2 channels. *Circ. Res.* 102:e54–e64. https://doi.org/10.1161/CIRCRESAHA.108.171736

Mori, M.X., M.G. Erickson, and D.T. Yue. 2004. Functional stoichiometry and local enrichment of calmodulin interacting with Ca2+ channels. *Science.* 304:432–435. https://doi.org/10.1126/science.1093490

Morotti, S., E. Grandi, A. Summa, K.S. Ginsburg, and D.M. Bers. 2012. Theoretical study of L-type Ca(2+) current inactivation kinetics during action potential repolarization and early afterdepolarizations. *J. Physiol.* 590:4465–4481. https://doi.org/10.1113/jphysiol.2012.231886

Neher, E. 1998. Vesicle pools and Ca2+ microdomains: new tools for understanding their roles in neurotransmitter release. *Neuron.* 20:389–399. https://doi.org/10.1016/S0896-6273(00)80983-6

O'Hara, T., L. Virág, A. Varró, and Y. Rudy. 2011. Simulation of the undiseased human cardiac ventricular action potential: model formulation and experimental validation. *PLOS Comput. Biol.* 7:e1002061. https://doi.org/10.1371/journal.pcbi.1002061

Peterson, B.Z., C.D. DeMaria, J.P. Adelman, and D.T. Yue. 1999. Calmodulin is the Ca2+ sensor for Ca2+ -dependent inactivation of L-type calcium channels. *Neuron.* 22:549–558. https://doi.org/10.1016/S0896-6273(00)80709-6

Pitt, G.S., R.D. Zühlke, A. Hudmon, H. Schulman, H. Reuter, and R.W. Tsien. 2001. Molecular basis of calmodulin tethering and Ca2+-dependent inactivation of L-type Ca2+ channels. *J. Biol. Chem.* 276:30794–30802. https://doi.org/10.1074/jbc.M104959200

Saucerman, J.J., and D.M. Bers. 2008. Calmodulin mediates differential sensitivity of CaMKII and calcineurin to local Ca2+ in cardiac myocytes. *Biophys. J.* 95:4597–4612. https://doi.org/10.1529/biophysj.108.128728

Stemmer, P.M., and C.B. Klee. 1994. Dual calcium ion regulation of calcineurin by calmodulin and calcineurin B. *Biochemistry.* 33:6859–6866. https://doi.org/10.1021/bi00188a015

Sun, H., N. Leblanc, and S. Nattel. 1997. Mechanisms of inactivation of L-type calcium channels in human atrial myocytes. *Am. J. Physiol.* 272:H1625–H1635.

Tadross, M.R., I.E. Dick, and D.T. Yue. 2008. Mechanism of local and global Ca2+ sensing by calmodulin in complex with a Ca2+ channel. *Cell.* 133:1228–1240. https://doi.org/10.1016/j.cell.2008.05.025

Tadross, M.R., M. Ben Johny, and D.T. Yue. 2010. Molecular endpoints of Ca2+/calmodulin- and voltage-dependent inactivation of Ca(v)1.3 channels. *J. Gen. Physiol.* 135:197–215. https://doi.org/10.1085/jgp.200910308

Tadross, M.R., R.W. Tsien, and D.T. Yue. 2013. Ca2+ channel nanodomains boost local Ca2+ amplitude. *Proc. Natl. Acad. Sci. USA.* 110:15794–15799. https://doi.org/10.1073/pnas.1313898110

Tang, Z.Z., M.C. Liang, S. Lu, D. Yu, C.Y. Yu, D.T. Yue, and T.W. Soong. 2004. Transcript scanning reveals novel and extensive splice variations in human l-type voltage-gated calcium channel, Cav1.2 alpha1 subunit. *J. Biol. Chem.* 279:44335–44343. https://doi.org/10.1074/jbc.M407023200

Downloaded from http://rupress.org/jgp/article-pdf/150/12/1688/1798053/jgp_201812115.pdf by guest on 09 February 2026

Tanskanen, A.J., J.L. Greenstein, B. O'Rourke, and R.L. Winslow. 2005. The role of stochastic and modal gating of cardiac L-type Ca2+ channels on early after-depolarizations. *Biophys. J.* 88:85–95. https://doi.org/10.1529/biophysj.104.051508

Teleman, A., T. Drakenberg, and S. Forsén. 1986. Kinetics of Ca2+ binding to calmodulin and its tryptic fragments studied by 43Ca-NMR. *Biochim. Biophys. Acta.* 873:204–213. https://doi.org/10.1016/0167-4838(86)90047-6

ten Tusscher, K.H., and A.V. Panfilov. 2006. Alternans and spiral breakup in a human ventricular tissue model. *Am. J. Physiol. Heart Circ. Physiol.* 291:H1088–H1100. https://doi.org/10.1152/ajpheart.00109.2006

ten Tusscher, K.H., D. Noble, P.J. Noble, and A.V. Panfilov. 2004. A model for human ventricular tissue. *Am. J. Physiol. Heart Circ. Physiol.* 286:H1573–H1589. https://doi.org/10.1152/ajpheart.00794.2003

Yazawa, M., M. Ikura, K. Hikichi, L. Ying, and K. Yagi. 1987. Communication between two globular domains of calmodulin in the presence of mastoparan or caldesmon fragment. Ca2+ binding and 1H NMR. *J. Biol. Chem.* 262:10951–10954.

Yin, G., F. Hassan, A.R. Haroun, L.L. Murphy, L. Crotti, P.J. Schwartz, A.L. George, and J. Satin. 2014. Arrhythmogenic calmodulin mutations disrupt intracellular cardiomyocyte Ca2+ regulation by distinct mechanisms. *J. Am. Heart Assoc.* 3:e000996. https://doi.org/10.1161/JAHA.114.000996

Zamponi, G.W., J. Striessnig, A. Koschak, and A.C. Dolphin. 2015. The Physiology, Pathology, and Pharmacology of Voltage-Gated Calcium Channels and Their Future Therapeutic Potential. *Pharmacol. Rev.* 67:821–870. https://doi.org/10.1124/pr.114.009654

Zühlke, R.D., G.S. Pitt, K. Deisseroth, R.W. Tsien, and H. Reuter. 1999. Calmodulin supports both inactivation and facilitation of L-type calcium channels. *Nature.* 399:159–162. https://doi.org/10.1038/20200

Downloaded from http://rupress.org/jgp/article-pdf/150/12/1688/1798053/jgp_201812115.pdf by guest on 09 February 2026